pnCCDs on XMM–Newton – fourty-two months in orbit

Lothar Strüder[1,3], Jakob Englhauser[1,3], Robert Hartmann[2,3], Peter Holl[2,3], Norbert Meidinger[1,3], Heike Soltau[2,3],
Ulrich Briel[1], Konrad Dennerl[1], Michael Freyberg[1], Frank Haberl[1], Gisela Hartner[1], Elmar Pfeffermann[1], Thomas Stadlbauer[1]

[1] *Max-Planck-Institut für extraterrestrische Physik, 85741 Garching, Germany*
[2] *PNSensor GmbH, Römerstr. 28, 80803 München, Germany*
[3] *MPI Halbleiterlabor, Otto-Hahn-Ring 6, 81739 München, Germany*

ABSTRACT

XMM–Newton – a cornerstone mission of the European Space Agency's Horizon 2000 programme – was launched on December 10, 1999 into orbit. Since March 2000 more than 2000 scientific observations were made. An example will be shown. The X-ray pnCCD camera on EPIC is operating since then without severe problems. We will report about the system performance as a function of time, with special emphasis on the effect of radiation damage in orbit. Up to now the spectroscopic and imaging performance of the pnCCD camera system is stable with time, even at the lowest energies most sensitive to degradation. The deviations of the detector response compared to the prelaunch performance over the 3.5 years is below 0.5%. One year after launch the pnCCD X-ray camera was hit by a micrometeoroid, damaging 35 pixels spread over the entire field of view. Details of the impact of the pnCCD with a cosmic dust particle will be given. X-ray fluorescence photons, stimulated by charged particles, constitute a significant part of the instrument background. Possible improvements for future missions will be discussed.

1. INTRODUCTION

The XMM–Newton X-ray observatory was successfully launched on December 10, 1999 from the European space port in Kourou, French-Guiana. The highly eccentric orbit with an initial inclination of 40° has a perigee of approximately 7000 km and an apogee of 120 000 km. During each 48 hour orbit XMM–Newton passes the Earth's radiation belts, resulting in a non-operational period of about 8 hours.

It is the aim of XMM–Newton to provide energy, position and time resolved X-ray data in the energy range from 150 eV up to 15 keV. For higher energies the efficiency of the mirrors rapidly drops below 1 cm^2. XMM is equipped with three individual Wolter-type I X-ray telescopes of 1500 cm^2 effective area, each with a focal length of 7.5 m. In addition to an optical monitor it carries two major instruments: A reflection grating spectrometer (RGS) and the European Photon Imaging Camera (EPIC). EPIC houses three individual X-ray CCD cameras as a wide field imager with a field of view of approximately 30 arcmin. Two MOS-CCD cameras are in the optical path of the telescopes with the gratings, where 50% of the incoming X-rays are deviated to the RGS readout. The pnCCD camera is in the focus of the unperturbated X-ray telescope with the full X-ray throughput. The properties of the pnCCD camera will be described in more detail in the next chapters.

As XMM–Newton is an observatory class mission it has to provide data to the broad band interests of the astrophysics community. That means it should be able to perform single photon imaging of extended objects and point sources. It should be capable to provide good timing of the X-rays in the order of several microseconds. High efficiency of the mirrors as well as of the detectors is essential. The highest possible energy resolution is required e.g. to measure precisely the abundances of elements, absorption features and temperatures. The non-imaging, energy dispersive RGS delivers a resolution of $E/\Delta E = 100$ to 500 from

0.3 to 3 keV. The imaging pnCCDs (and MOS-CCDs) have a factor of 10 less energy resolution; however, the upper energy response extends to about 15 keV. In that sense every instrument has its own merits.

To date, after 42 months of operational experience we have learned that the stability of the instrument is a value of its own. The detector properties should not vary with time because a wide community of physicists (approximately 1500 from 36 countries) are constantly processing data from the early stage of the mission up to now. A calibration team of about 30 physicists is routinely comparing the measured data with the calibration data. The observation time is distributed through an "Announcement of Opportunity" and the observational requests are evaluated through a science panel. Typically a factor of 8 times more observation time is asked for by the scientific community than can be provided by the programme committee.

We will briefly describe the pnCCD camera concept and highlight a typical observation. Calibration and background issues will be emphasized. The effect of radiation damage including a micrometeoroid impact with the X-ray telescope and the sensor will be analysed in detail.

2. A BRIEF REVIEW OF THE PNCCD PRINCIPLES AND PROPERTIES

The principle of sideward depletion in high resistivity silicon is the basis of a large variety of novel silicon detectors, such as silicon drift detectors,[1] controlled drift detectors, active pixel sensors — and pnCCDs.

2.1. The camera concept

The angular resolution of the XMM X-ray telescope in front of the pnCCD camera is 15 arcsec half energy width (HEW) at 1.5 keV and 8 keV. This translates to 540 μm position resolution required in the focal plane. For a given telescope performance the concept of sideward depletion allows for an optimum adaption of the pixel size to the X-ray optics, varying from 30 μm up to 300 μm. The FWHM of the point spread function (PSF) is 6.6 arcsec. A pixel size of 150 μm$\times$150 μm (4.1 arcsec) was chosen, with a position resolution of 120 μm, resulting in an equivalent angular resolving capability of 3.3 arcsec.[2] The energy response is higher than 90% at 10 keV because of the sensitive thickness of 300 μm. The low-energy response is given by the very shallow implant of the p^+ back contact; the effective "dead" layer[3] is of the order of 300 Å. High time resolution is a consequence of the parallel readout of 64 channels per subunit, 768 channels in total for the entire camera. High radiation hardness is built in by avoiding active MOS structures and by the fast transfer of the charge in a depth of more than 10 μm below the surface.

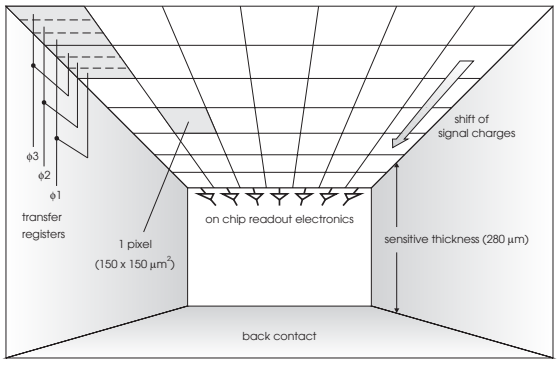

Figure 1. *Inside the pnCCD. The X-rays hit the device from the backside (bottom). The charges are collected in the electron potential minimum 10 μm from the surface having the pixel structure. After integration, they are transferred to the on-chip amplifier. Each CCD column is terminated by an on-chip JFET amplifier.*

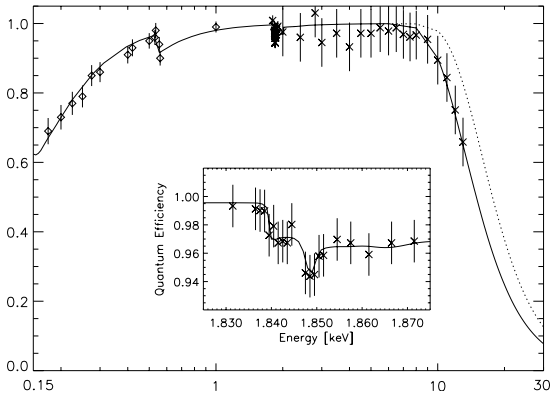

Figure 2. *Quantum efficiency (QE) of the pnCCD with a fully depleted thickness of 300 μm. The inset depicts in more detail the response of the pnCCD around the Si-K edge measured through PTB at BESSY. The energy scale ranges from 150 eV to 30 keV. The solid and dotted lines represent the best-fit models for a sensitive volume of 300 μm and 500 μm thickness, respectively.*

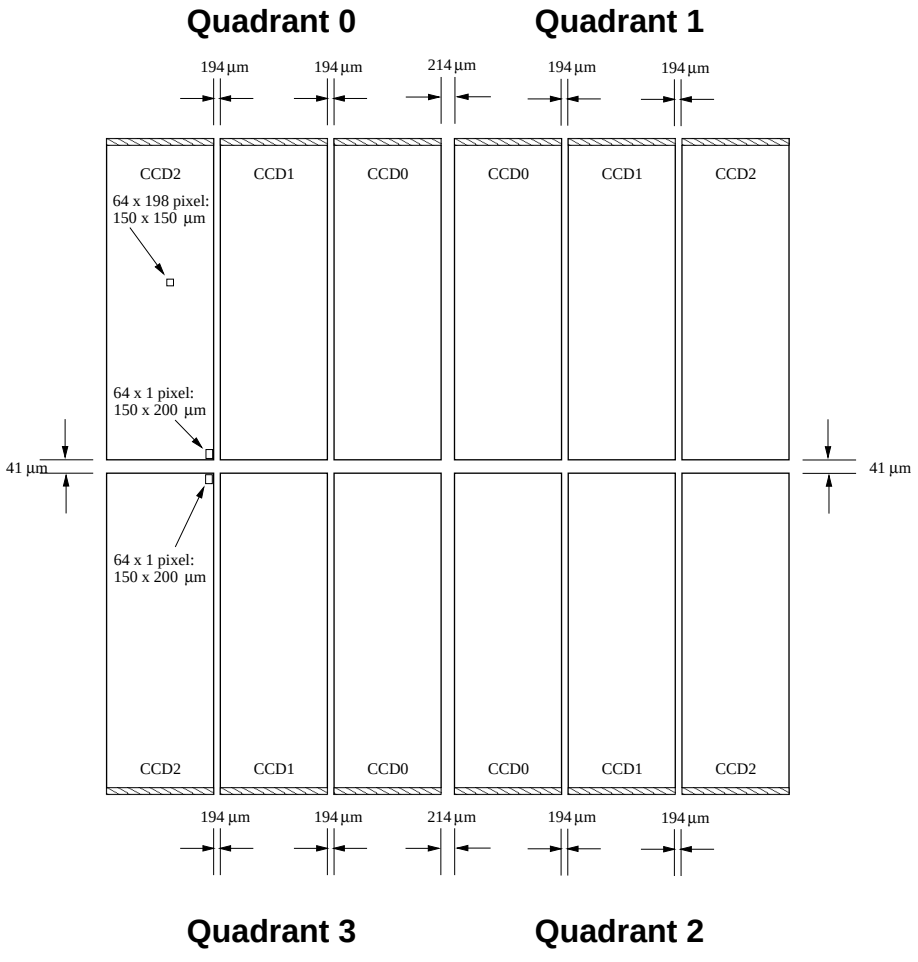

Figure 3. *Overview of the internal boundaries of the pnCCD focal plane. The division of the focal plane in subunits was made because of redundancy reasons. The focal point of the X-ray telescope is in CCD0, quadrant 1. About 97% of the telescope's field of view is covered by the focal plane. About 6 cm^2 of the CCD's sensitive area are outside the field of view and is used for background studies. The world's largest X-ray CCD with a sensitive area of 36 cm^2 was fabricated in the MPI - semiconductor laboratory.*

2.2. The basic principles of pnCCDs

The schematic view into the pnCCD in Fig. 1 already introduces intuitively the advantages of the concept: X-rays hit the detector from the rear side. In case of an X-ray interaction with the silicon atoms, electrons and holes are generated. The average energy required to form an electron-hole pair is 3.7 eV at -90° C. The strong electric fields in the pnCCD detector separate the electrons and holes before they recombine. Signal charges (in our case electrons), are drifted to the potential minimum and stored under the transfer registers. The positively charged holes move to the negatively biased back side, where they are 'absorbed'. The electrons, captured in the potential wells 10 μm below the surface can be transferred towards the readout nodes upon command, conserving the charge distribution from the ionization process, including the electrostatic repulsion and diffusion of the signal charges during their drift to the local potential minimum. As can be seen in Fig. 1, each CCD line is terminated by a readout amplifier. The focal plane layout is depicted in Fig. 3. Four individual quadrants – monolithically integrated on a 4 inch wafer – each having three pnCCD subunits with a format of 64×200 pixel are operated in parallel.[4]

The spatially uniform detector quality over the entire field of view is realized by the monolithic fabrication of 12 individually operated 1×3 cm^2 pnCCDs on a single wafer (see Fig. 3). No inhomogeneities were observed in the tested energy range from 700 eV up to 8 keV, the measured flatness of the homogeneity measurements was always limited by Poisson statistics. Fig. 3 shows the insensitive or partially sensitive gaps in between the different CCDs and quadrants. As all CCDs are monolithically integrated on a single 4 inch wafer, the relative adjustment of the chips, i.e. all pixels, is known with a precision of better than 1 μm. The

Table 1. Parameters of the six standard readout modes as implemented in-orbit (FF: full frame, eFF: extended full frame, LW: large window, SW: small window, TI: timing, BU: burst). The energy flux at which pile-up becomes relevant (last column*) was derived in the energy band from 0.1 keV to 10 keV, assuming an unabsorbed power law with photon index 2.0, observed with the thin filter.

mode	field of view (FOV) in pixel format in arc min.	time resolution in ms	out of time (OOT) events in %	life time with OOT events in %	brightest point source for XMM in counts s^{-1} in erg cm^{-2} s^{-1} *
FF	398 × 384 27.2 × 26.2	73.3	6.2	100	6 8.1×10^{-12}
eFF	398 × 384 27.2 × 26.2	199.2	2.3	100	for extended sources only
LW	198 × 384 13.5 × 26.2	47.7	0.15	94.9	9 1.2×10^{-11}
SW	63 × 64 4.3 × 4.4	5.7	1.1	71.0	100 1.4×10^{-10}
TI	199 × 64 13.6 × 4.4	0.03	100	100	4000 5.9×10^{-9}
BU	20 × 64 1.4 × 4.4	0.007	depends on PSF	3.0	60 000 8.1×10^{-8}

separation of the large CCD into quadrants and individual $1 \times 3\,cm^2$ pnCCDs on a wafer was done because of redundancy reasons.

The detector is cooled to suppress the thermally generated leakage current. We have chosen a temperature of -90° C, reducing the leakage current to less than 0.1 e^- per pixel and per readout cycle of 73 ms. Taking into account the residual partial pressure inside the camera of less than 10^{-5} mbar, formation of monolayers of e.g. ice on the radiation entrance window should not occur at that temperature. Also for safety reasons the operating temperature was chosen to be as high as -90° C to prevent delamination of the multilayer printed circuit boards (PCB). Our operating temperature is typically 30 K warmer than compared to the MOS cameras on XMM–Newton and Chandra, which had to lower the operation temperature because of radiation damage issues. For the pnCCD camera there is no indication for the need of a change of the temperature, keeping the calibration constant throughout the mission.

3. OBSERVATIONS

Since the end of the calibration and test phase the pnCCD camera performed more than 2000 independant observations with a duration between 1000 and 1 000 000 seconds. In most of the cases the pnCCD camera was chosen as the prime instrument. A typical example of such an observation is shown in Fig. 4. The remnant of the type Ia supernova explosion noticed by Tycho Brahe in November 1572 was observed by XMM–Newton on June 29, 2000 at the end of the calibration phase. With its age of 431 years, Tycho's SNR is still expanding almost undecelerated by the ambient medium. The X-ray emission is dominated by the shocked ejecta in a spherical shell of about 8 arcmin angular diameter. EPIC-PN data from 0.2 keV to 12 keV were used to construct an intensity image. After removing background and out-of-time events the mean photon energy is in the range of 1.2 keV.

The X-ray spectrum integrated over the entire remnant is dominated by the emission lines of highly ionized Ne, Mg, Si, S, Ar, Ca and Fe in various ionization stages (Figs. 4 to 8). These data were used e.g. to analyse the kinematics of the ejecta and their velocity distribution. The dynamics of the explosion could thus be studied in detail.[5]

Some highlights of other observations being possible only because of the special pnCCD features include (a) the observation of z=6 quasars making use of the high quantum efficiency at low X-ray energies, (b) the observation of millisecond pulsars because of the high time resolution and (c) the observation of very strong sources because of the fast readout.

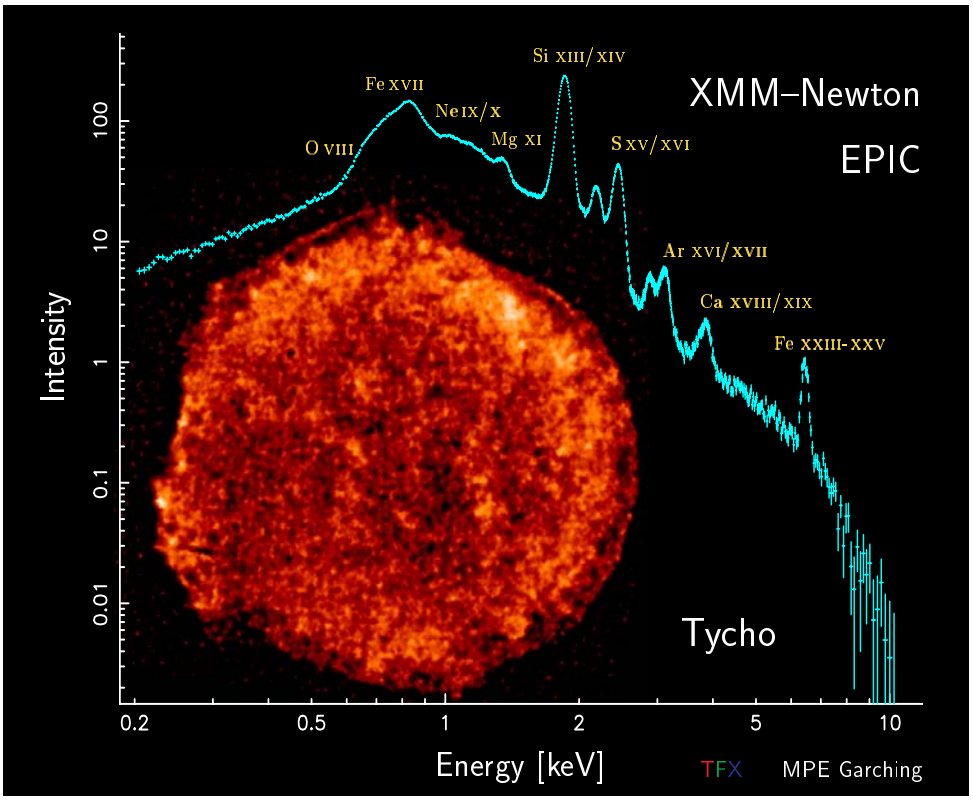

Figure 4. *The remnant of the supernova first seen by Tycho Brahe in 1572. With its age of 431 years, Tycho's SNR is still expanding almost undecelerated by the ambient medium. The X-ray emission is dominated by the shocked ejecta in a spherical shell of about 8 arcmin angular diameter. EPIC-PN data from 0.2 keV to 12 keV were used to construct this intensity image. The azimuthal variation of the expansion rate points out the high velocity of the blast wave in the west (to the right) with a value of 7000 km/s, assuming a distance of D=3 kpc. The mean radius of the outer shock front corresponds to a radial extent of 3.64 pc.*

4. CALIBRATION AND BACKGROUND ISSUES

The calibration of the pnCCD camera was made at the synchrotrons BESSY in Berlin under the leadership of PTB, at LURE in Orsay, and at the MPE PANTER test facility in Neuried.

Just before diving into the Earth's radiation belts, the scientific observations are discontinued and a movable shutter prevents the camera from radiation damage. During the travelling time in the belts an internal calibration source (^{55}Fe) is moved into the field of view, generating the Mn-K_α and Mn-K_β lines at 5.9 keV and 6.5 keV, and an Al-K_α line at 1.48 keV by irradiating an Aluminum target. They can be seen in Fig. 9 as the most prominent lines.

The pnCCD camera system was submitted to an intensive ground calibration programme. A detector response matrix was filled with measured data and modelled interpolations, where no data were available. Within the measurement accuracy the in-flight performance does not deviate from ground calibrations under the same operating conditions.[6]

4.1. Quantum efficiency

The fully depleted 300 μm of silicon determines the detection efficiency on the high energy end, while the quality of the radiation entrance window is responsible for the low energy response. The entire bandwidth is essential for the mission. Fig. 2 shows the result of the absolute quantum efficiency calibration at PTB (BESSY synchrotron in Berlin) and LURE (synchrotron in Orsay, Paris).[7] All measurements were made under conditions comparable to space operation. The drop of quantum efficiency (QE) at the lowest energies is caused by the properties of the silicon L-edge. The absorption length of X-rays in silicon at e.g. 150 eV is only 30 nm. A thin oxide layer of the order of 20 nm already absorbs about one half of the incident photons.

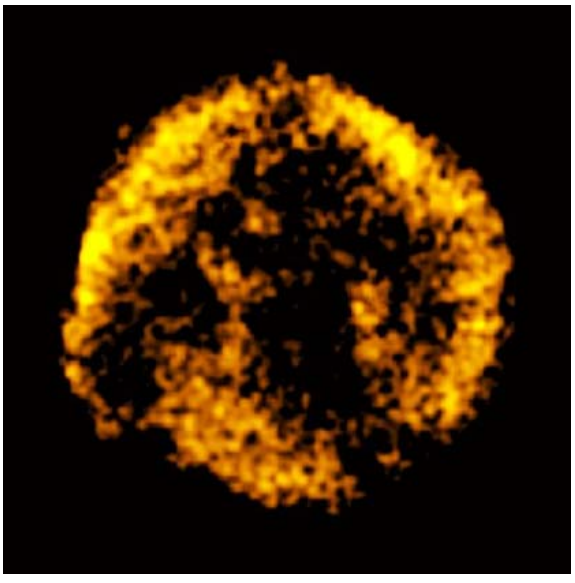

Figure 5. *Mg line intensity of the Tycho SNR.*

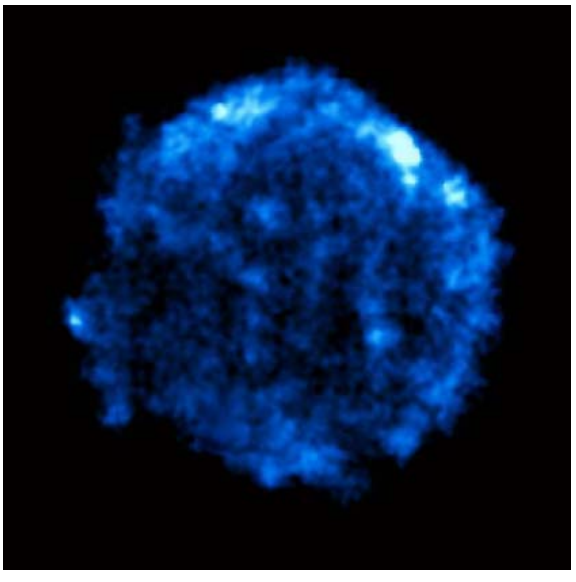

Figure 6. *Si line intensity of the Tycho SNR.*

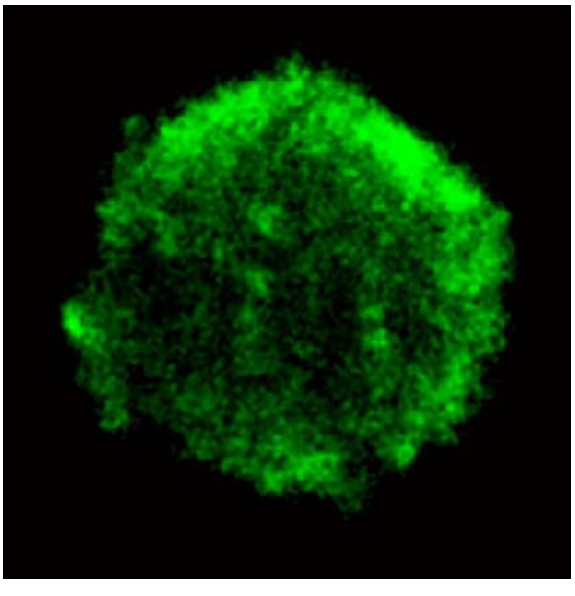

Figure 7. *S line intensity of the Tycho SNR.*

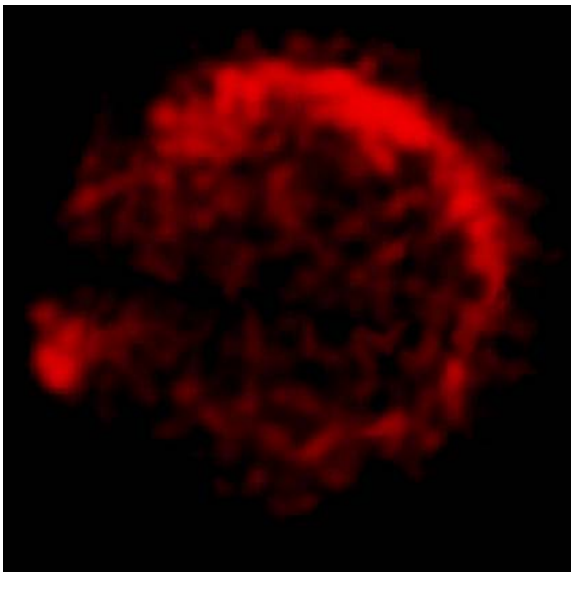

Figure 8. *Fe line intensity of the Tycho SNR.*

The drop of about 5% of QE at 528 eV is due to the additional absorption in the SiO_2 passivation on the detector surface. The other prominent feature in Fig. 2 is the typical X-ray absorption fine structure (XAFS) behaviour around the silicon K edge at 1.838 keV, enlarged in the inset of Fig. 2. At higher energies the model (solid line) nicely fits the photon absorption data for 300 μm of silicon. The QE is not supposed to change during the XMM lifetime under nominal conditions. This is different for all other CCD-type cameras on ASCA, Chandra, and XMM–Newton.

4.2. Energy resolution

The energy resolution is mainly determined by the statistical fluctuations of the ionization process (Fano noise), the charge transfer properties of the CCD and the electronic noise of the readout node.[8] Fig. 9 shows about 31 hours of in-orbit data with the internal calibration source (^{55}Fe), and with the filter wheel in closed position.[9] The signals selected are only those which hit the CCD in the last 20 lines of the 12 CCDs, the area, which also contains the focal point. X-ray events from this region have undergone the maximum number of pixel transfers and therefore the highest charge losses. The Al-K_α, Mn-K_α and Mn-K_β fluorescence lines and the Mn-K_α escape peak are clearly visible. The Cu-K_α and Cu-K_β peaks are fluorescence lines from the printed circuit board, generated by ionizing particles traversing the whole pnCCD camera. The other fluorescence lines (e.g. K-K_α, Ti-K_α, V-K_α, Cr-K_α, Fe-K_α, Ni-K_α, Zn-K_α) are trace elements in the aluminum structure of the camera and the invar ring holding the pnCCD wafer. Those X-rays constitute a

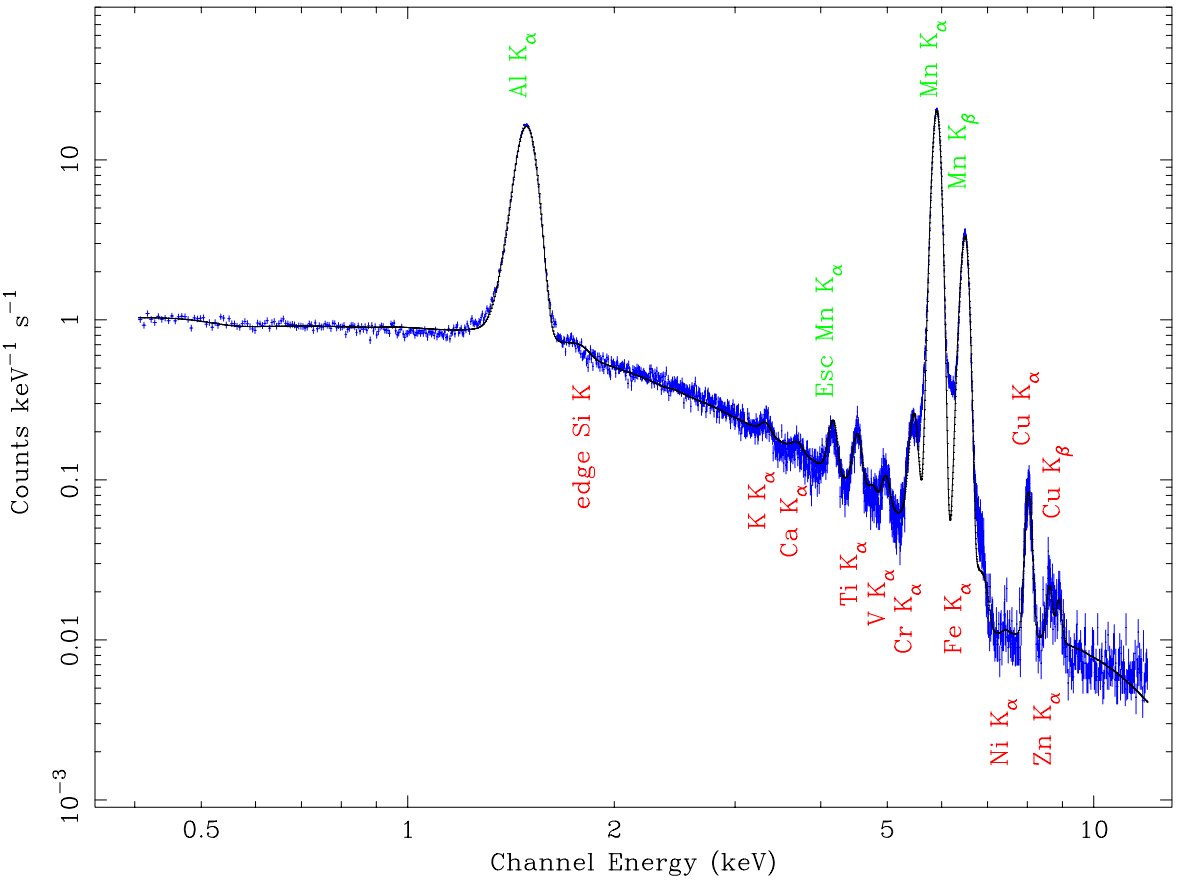

Figure 9. *Calibration spectrum with the internal radioactive source including the background with the filter wheel in closed position. The continuous background below the Mn lines arises mainly from photoelectrons stimulated from the* ^{55}*Fe source in the Al target. The Fe-*K_α *line between Mn-*K_α *and Mn-*K_β *is not resolved. The additional lines are due to X-ray fluorescent background from the camera structure.*

significant fraction of the instrument background. The energy resolution in the full frame mode is extracted from the internal calibration source including all kind of X-ray background. At Mn-K_α the FWHM is 161 eV in the focal point, it is 152 eV averaged over the whole CCD and is 140 eV close to the readout nodes. The energy resolution improves in the extended full frame mode to 148 eV (FWHM) averaged over the entire chip. The Al-K_α resolution is 111 eV (FWHM) for the full frame and 105 eV in the extended full frame mode.

The long term instrument stability is checked routinely in terms of housekeeping data from all relevant camera parameters, and by analysing the spectroscopic performance of the on-board calibration source and celestial sources.[10] Fig. 16 shows the variation of the Mn-K_α resolution as a function of time after launch. The increase of the FWHM is compatible with the slight worsening of the charge transfer. As 1 ADU corresponds to 5 eV, the increase of the energy resolution varies between 1 eV and 1.5 eV per year as expected.[11] The intrinsic stability of the instrument (stability of peak position, stability of quantum efficiency, homogeneity of the X-ray response) is better than 1%.

The 768 on-chip readout amplifiers are operated in a "self rest" mode.[12] When heavily ionizing radiation hit the detector releasing many electrons in a single pixel (e.g. more than 500 000 electrons), the long settling time of the auto-reset perturbates the reading of the successing pixels, generating false signal amplitudes. This could be remedied by applying a reset on command, whenever a signal charge above a given threshold was detected. This was not foreseen on XMM.

The pnCCD onboard XMM–Newton is operated in a 'full frame' mode. This includes that X-rays hitting the CCD during readout are assigned with the wrong position in the transfer direction. Those hits are

called "out-of-time" events. In the full frame mode 6.2% of the X-rays are distributed along the transfer direction. As their real hit position is not known, corrections of the charge transfer efficiency (CTE) cannot be applied. In future applications a frame store area will be added to the image area. A fast transfer of the signal charges from the image to the store section suppresses the amount of out-of-time events by the ratio of image integration time to the transfer time from the image to the store area. This technique will be applied e.g. for the pnCCDs aboard the ROSITA mission.[13]

4.3. Instrument background

As can be seen in Fig. 9 two other features of the spectrum need some explanation. (a) The continuous background from the lowest energies up to the Mn-K lines. This background is due to photo electrons from the Al fluorescence target, excited from the Mn-K X-rays from the calibration source. Because of the very thin radiation entrance window of the pnCCD the low energy electrons can be clearly detected with high QE. This property is equally responsible for the high QE response for soft X-rays. (b) The flat background distribution for the highest energies arises from Compton electrons, generated by X- and gamma rays.

Another source of instrument background is caused by particles from the solar wind, being locally trapped in the Earth's magnetosphere. They can be light and heavy ions as well as highly ionizing low energy protons.[14] The background level changes with timescales of minutes to hours, as the spacecraft passes the trapped particles. The occurence of these flares is unpredictable.[6] The particles are being imaged upon the detector by means of grazing incidence reflection through the X-ray telescope.

The pnCCD camera has the option to lower the gain of the signal processing electronics by a factor of 20, in order to increase the dynamic range to about 300 keV. This mode is very useful to study background phenomena. The results of the analysis of those "soft solar proton flares" can be summarized[15] as follows:

1. The energy distribution of the protons has its maximum at the lowest measured energies at 1 keV with an exponential attenuation of 4 orders of magnitude at 200 keV.
2. The protons show a clear vignetting, proving that they have been imaged through the telescope.
3. The protons loose typically 50 keV of energy in the thick filters and about 20 keV in the thin filters.
4. The soft proton flares heavily load the observational background (and the satellite telemetry) and therefore disturb and limit the observations, but they do not damage our instrument.

Minimum ionizing particles (mips) traverse the detector and leave about 80 electron-hole pairs per μm track length in the silicon. In a Monte-Carlo simulation we assumed a 4π isotropic distribution of the mips, which nicely fits the measured data[15]: The average energy deposition in one pixel is in the order of 50 keV and the average number of pixels involved in a mip track is about 10. The most probable track length in one single pixel is 150 μm. The onboard processor is able to remove almost 100% of the mips. Post-processing on ground is then required to reject 100% of the mips. Figs. 10 and 11 show one example of the X-ray fluorescence effects in the camera itself, generated by charged particles going through the camera..[16] The printed circuit board in Fig. 10 carries the 4 inch CCD wafer. The wafer is mounted on an invar ring at a distance of about 250 μm from the PCB. The PCB itself has 14 conduction layers individually organized in the four different quadrants. All conductive layers are made of copper and molybdenum. After measuring about 30 hours of background we get a projection of the Cu-K_α X-rays from all the layers of the PCB onto the pnCCD. The readout chips (CAMEX) are located at the top and the bottom in Fig. 11. The big oval shaped opening in the center is clearly to be seen. Even the four smaller holes, two at the right and two at the left hand side, can be found in the PCB of Fig. 10. Similar images have been made with other prominent lines from the spectrum of Fig. 9. This way the origin of the fluorescent X-rays can be traced back to the camera geometry and the used materials. In future camera designs we will make use of graded shielding techniques to minimize fluorescent X-rays to reach the detector.

The instrument background was determined by measurements in orbit with the filter wheel closed. In the energy band of 2 keV to 10 keV a single-pixel event flux of 4.5×10^{-4} s^{-1} keV^{-1} arcmin^{-2} was measured. For a circle with a radius of 7 arcsec – i.e. the half energy width of the telescope system – this reduces to 1.5×10^{-4} events/s. The cosmic X-ray background within the 7 arcsec radius is 2.3×10^{-5} singles/s. A circle with a radius of 7 arcsec characterizes the half energy width of the telescope and therefore gives a background estimate for a point source.

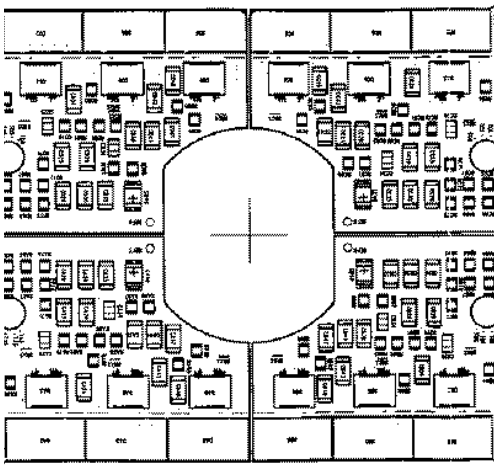

Figure 10. *Multilayer printed circuit board separated by 0.25 mm from the X-ray CCD. The PCB has conductive layers of copper which can be excited by the ionizing radiation in the XMM orbit. This way Cu-K_α and Cu-K_β fluorescence X-rays are projected on the pnCCD. The inner oval shaped opening in the PCB can clearly be identified (magnified) in the center of the CCD image in Fig. 11.*

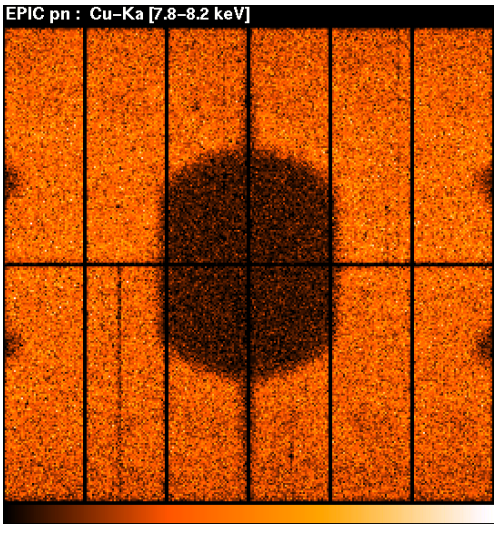

Figure 11. *X-ray fluorescence image of the Cu-K_α X-rays (7.8 – 8.2 keV) on the CCD. Those photons correspond to the Cu peak in the calibration spectrum of Fig. 9. All those events contribute to the instrument background which cannot be distinguished from cosmic X-rays.*

In a more optimized set-up for a different application[17] we have achieved a background level (on Earth) of 1.5×10^{-4} events s^{-1} keV^{-1} cm^{-2} which translates to more than a factor of 60 less background. This is a factor of 10 less than the cosmic X-ray background.

The analysis of the radiation background of all kinds will be an ongoing activity because of the lack of precise predictability, time transients and missing knowledge about the composition, energy profile, and spatial distribution in the XMM orbit.

5. RADIATION DAMAGE

The orbit of XMM–Newton is flooded by solar protons, such that after a 10 year operation and an effective shielding of the camera by an equivalent of at least 3 cm aluminum, the sensor will finally face the damage by 5×10^8 protons per cm^2 of 10 MeV. A large variety of tests was made to study the radiation damage as a function of fluence, energy, operating temperature, operating conditions and as a function of the radiation type.

For low energy protons, imaged through the X-ray optics[14] the pnCCD is "self shielding", because they cannot propagate through 290 μm of silicon and damage the transfer channel. Therefore the charge transfer efficiency is not affected by low energy protons. A proton energy of about 7 MeV is required to pass through 290 μm of silicon. As there is only a negligible transmission of protons through the X-ray optics above 500 keV, there is no problem for the pnCCD with low energy protons at all.[18] For those tests 1.4×10^9 protons per cm^2 were irradiated onto the pnCCD's entrance window. No change of the detector properties was seen. This proton irradiation was made at energies between 1 keV and 300 keV with prominent peaks at 70 keV and 170 keV.

Measurements in a proton accelerator[19] with up to 2×10^9 10 MeV protons per cm^2, equivalent to 4 times the expected 10 year XMM irradiation in space, only showed a degradation of about 30 eV in the FWHM of the Mn-K_α line. Up to now, no unexpected degradation due to radiation damage was found in orbit. Figs. 12 and 13 show the compiled results of the prelaunch damage tests with 10 MeV protons. According to Fig. 13 the energy resolution should degrade from 145 eV at an operating temperature of 174 K to 163 eV after 10 years of operation. As we are operating at 183 K the measurable damage should be slightly lower. In fact we have seen up to now an increase of FWHM of the Mn-K_α of about 1 eV per year. The increase

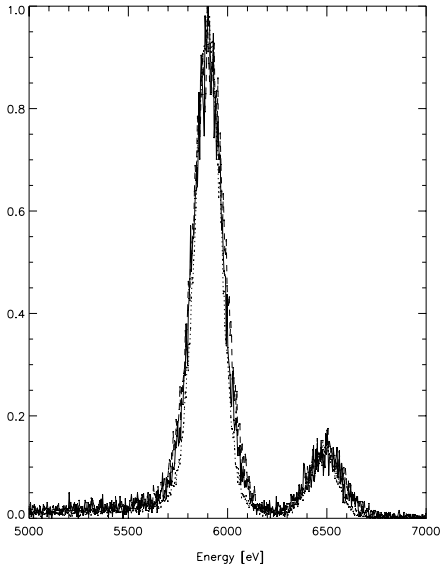

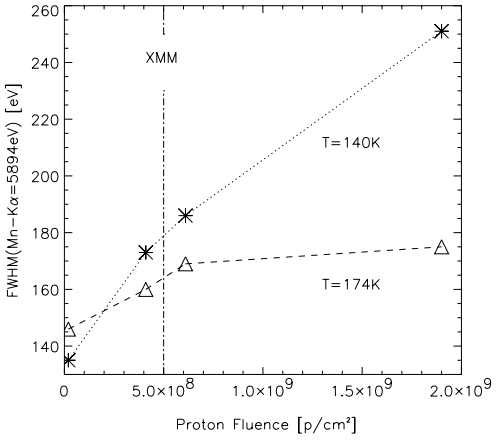

Figure 12. ^{55}*Fe energy spectrum after different 10 MeV proton fluences of 0 p/cm^2 (dotted line), 4.1 · 10^8 p/cm^2 (solid line), 6.1 · 10^8 p/cm^2 (dashed line), measured at the low (and after irradiation unfavourable) temperature of 142 K. The expected dose over a life time of 10 years is 5 · 10^8 10 MeV p/cm^2.*

Figure 13. *FWHM of the Mn-K_α-line (5.9 keV) in dependence on proton fluence and temperature. Before proton exposure the lower operating temperature of 140 K gains better results. After a 10-MeV proton fluence of more than 2 · 10^8 cm^{-2} the higher temperature of 174 K results in a better energy resolution. The FWHM is degraded from 135 eV (140 K) to 160 eV and 175 eV (174 K) after 4.1 · 10^8 p/cm^2 and 1.9 · 10^9 p/cm^2 respectively. A FWHM of 160 eV is expected after the 10 year XMM mission.*

of the energy resolution of the Al-K_α line seems to be less. The radiation damage mainly occurs through "A centers" (Oxygen-Vacancy defect at 0.17 eV below the conduction band) capturing and releasing signal electrons during the transfer.[19] The increase of leakage current per 10 MeV proton at room temperature was approximately 10^{-17} A. At our operating temperature this does not contribute to the measured noise.

Figs. 14 and 15 show the increase of charge transfer inefficiency (CTI) over the last 3.5 years for the Al and Mn X-ray lines, i.e., 1.0×10^{-5} and 1.4×10^{-5} per year. We correct off-line for the changing CTI. The related effect on the energy resolution is shown in Fig. 16.

6. MICROMETEOROID IMPACT

A different kind of damage occurred during revolution number 156 when a sudden increase of count rate indicated a local formation of bright pixels.[20] About 35 pixels were involved. The 35 pixels were hit simultaneously, randomly distributed over one half of the focal plane. The locally generated leakage current was by far too high to be explained by heavy ions. The only instant remedy was to set the affected pixels 'bad'. An analysis of all instrumental effects has clearly shown, that no other explanation than a micrometeoroid deflected through the X-ray telescope and eventually hitting the CCD was able to consistently explain the measurements.

We used the dust accelerator of the MPI für Kernphysik in Heidelberg to analyse the dust reflection off the mirror shells and the damage of the detector in detail[21]: An XMM mirror segment was put into the

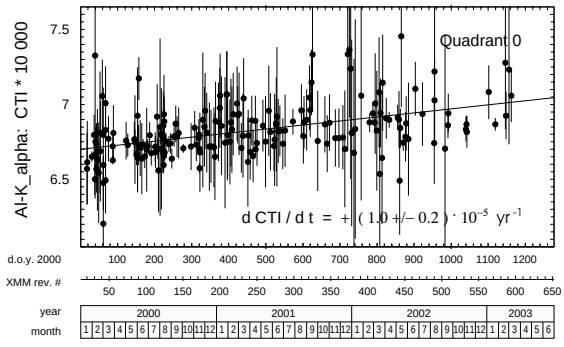

Figure 14. *In-orbit measurements of the CTI at the Al-K_α line. The large error bars are due to measurements with poor statistics. The CTI increase is 1×10^{-5} per year.*

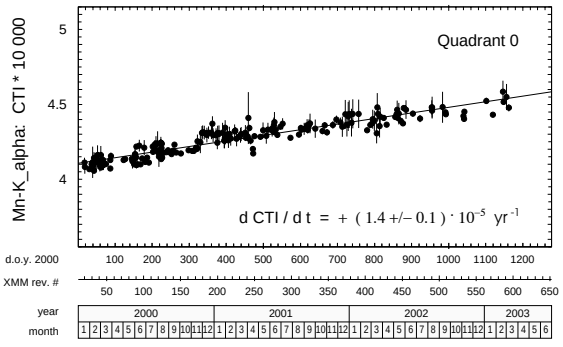

Figure 15. *In-orbit measurements of the CTI at the Mn-K_α line. The CTI increase is 1.4×10^{-5} per year. This explains the decrease of energy resolution of 1 eV per year.*

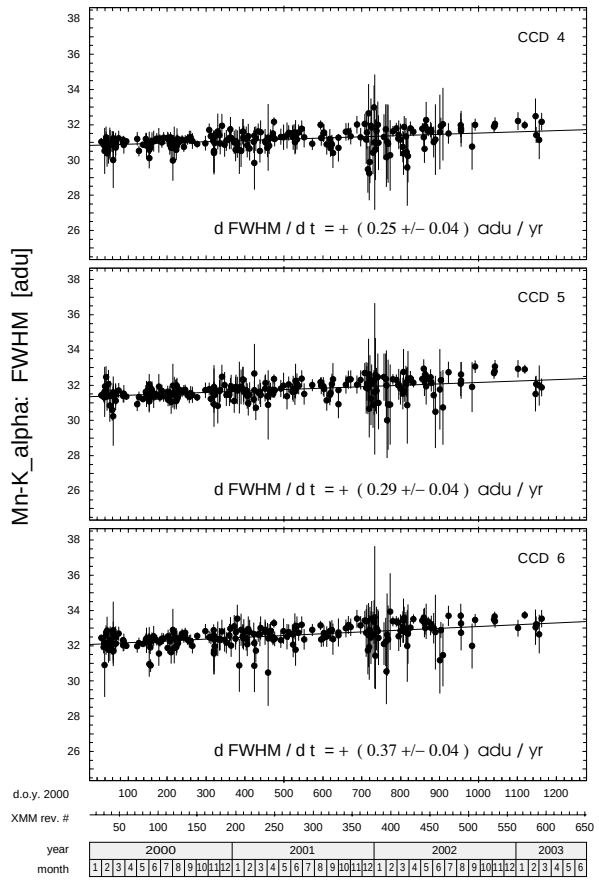

Figure 16. *Changes of energy resolution over the first 3.5 years. The partially large error bars are the result of short calibration measurements, i.e. low statistics.*

trajectory of the microscopic iron particle. Behind the mirror the pnCCD was placed to study the impact on-line. We have observed, that the reflection off the mirror shells is highly efficient up to angles of about 4 degree, the maximum angle we could realize in our test set-up. In general the output angle is much smaller than the input angle, accounting for the inelastic scattering process on the gold mirror surface. We did not find any gold on the detector surface and in particular not in the impact craters.

Figs. 17 and 18 show a scanning electron microscope (SEM) image of an impact area. A typical crater core of a size of about $2\times2\times3\,\mu\mathrm{m}^3$ was found if the incident massive iron projectiles have typical diameters

of 0.2 μm to 2 μm at velocities of 5 km/s. The mass of the iron particles varies between 10^{-13} g and 10^{-10} g.

A simple model can be used to estimate the local temperature at the micrometeoroid hit location within e.g. 1 μs after the impact. During that time only the mechanically damaged area notices the increase of temperature ΔT within the volume of the crater.

$$\Delta T = \frac{Q}{c_{si} \cdot m_{si}} \approx \frac{m_{fe} \cdot v^2}{2} \cdot \frac{1}{c_{si} \cdot m_{si}}$$

$$\Delta T = \frac{4\pi \cdot r_{fe}^3 \cdot \rho_{fe} \cdot v^2}{3 \cdot 2} \cdot \frac{1}{c_{si} \cdot l_{si}^3 \cdot \rho_{si}}$$

ΔT is the local temperature increase, Q the deposited energy, c_{si} and m_{si} the specific heat capacitance and mass of the heated silicon. m_{fe} denotes the mass of the iron particle and v its velocity. r_{fe} is the radius of the iron particle and ρ_{fe} the specific weight and l_{si} approximates the volume of the affected silicon with an edge length of l_{si}.

With a specific heat capacitance of 700 J/kg·K, $r_{fe} = 0.3\,\mu$m, $l_{si} = 2\,\mu$m, and a particle velocity of 5 km/s, the temperature increase at the impact point will reach values of 850 K. Under those typical conditions the local temperature rises for a short moment to 1030 K. Fig. 20 shows the consequence of the sudden heat-up: the readout frame during which the impact happened, shows a halo of infrared light due to the local temperature increase around the craters. The IR halo completely disappears in the subsequent frame. The IR light has a long absorption length in silicon and may propagate several mm in the pnCCD before being converted. The thick silicon (0.3 mm) and the lateral extension of the IR light cone over several mm (see Fig. 20), make it highly probable that at T $\approx$ 1000 K we get sufficient signal IR light to detect it in the pnCCD. The QE at 1.1 μm is still above 80%.

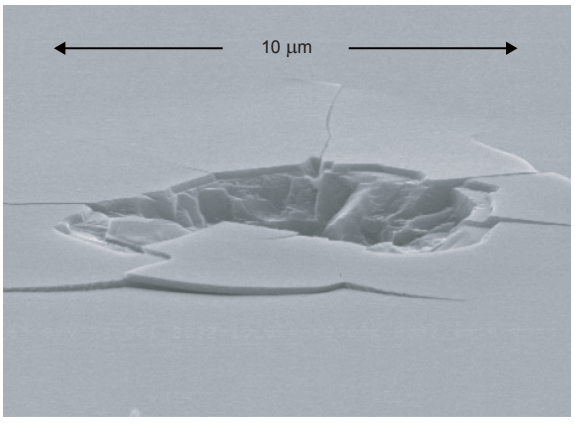

Figure 17. *Micrometeoroid impact crater from a particle of approximately 1 μm size. The craters may have a lateral extension of up to 10 μm. As can be seen, microcracks in the 0.2 μm thick SiO_2 can extend laterally to more than 15 μm.*

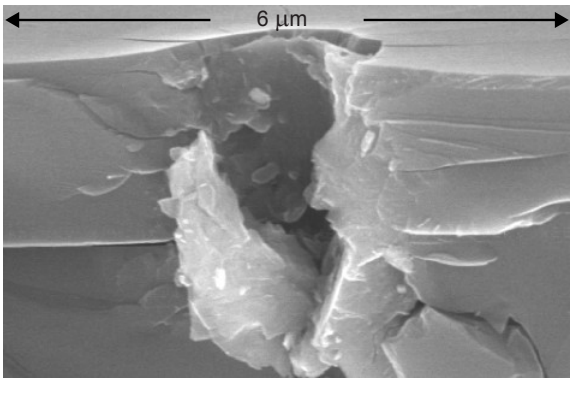

Figure 18. *Cut through a micrometeoroid impact crater. The depth can be as much as 3 μm. No cristalline Si splinters are found. The damage in the monocrystalline structure is much more extended.*

As discussed previously, during the impact (less than 1 μs) the temperature rises up to values above 1000 K making the moment of the impact comparable to a thermo-mechanical explosion. The short moment of the high temperature leads to the emission of infrared light, which is recorded in the readout frame of the impact (see Fig. 20). As silicon is a very good heat conductor at low temperatures, this effect disappears in the next frame 70 ms later. As the thermally generated infrared light has a very long absorption length in silicon, it can be seen in a large halo around the crater, before the non-converted infrared light leaves the pnCCD.

The SEM was equipped with an X-ray detector for the chemical analysis of the surface of craters. In some cases we found residuals of iron at the edges of the crater (Fig. 19). We did not find any abundances of Al and Au in the craters or their vicinity.

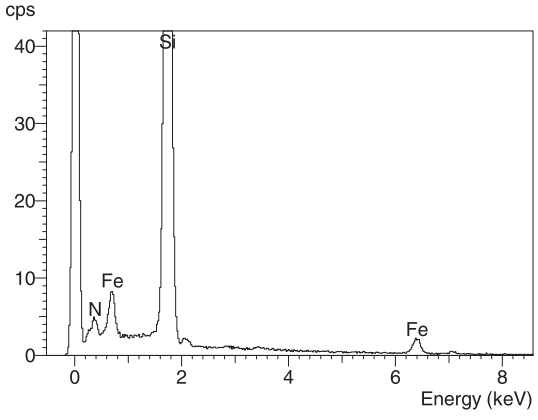

Figure 19. *X-ray fluorescent spectrum of the scanning electron microscope image of Fig. 17. Beside a strong silicon and nitrogen peak from the CCD it also shows a clear iron -K_α and -L_α peak, proving that a piece of the incident iron dust particle was scattered off the mirror shell and reached the pnCCD.*

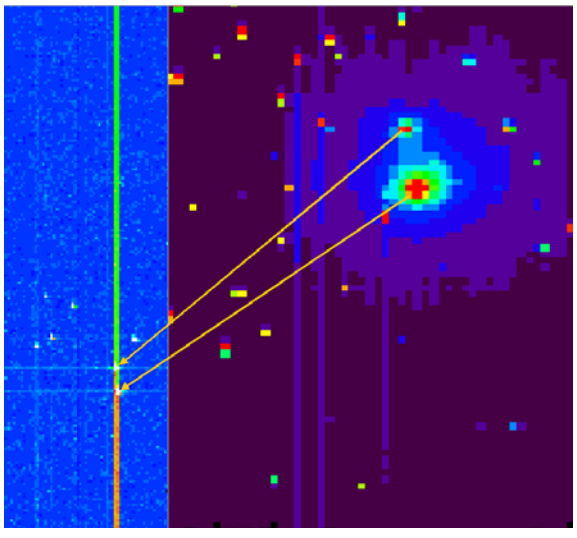

Figure 20. *The left part of the figure (blue) shows the 3×1 cm^2 with the recently generated impact craters. The affected columns show a dramatic increase of leakage current. The image on the right hand side is a zoom of the latest impacts. The light "halo" around the two craters is nicely seen.*

During the first 3.5 years of operation in total 3 impacts occurred on XMM at three different times, once in each of the PN, MOS1 and MOS2 cameras. The total loss in sensitive area is of the order of 10^{-4} which does not at all affect the science. But if more critical orbits would be chosen (e.g. low earth orbits) or if the mirror size would be increased substantially (see XEUS, Constellation X) micrometeoroid impacts could be much more frequent and reduce the life time of the missions.

To better understand the physics of the micrometeoroids a study group was formed at ESA to theoretically and experimentally analyse all aspects of the encounter of (dust) particles with the scientific instruments in space.

7. CONCLUSIONS

The pnCCD camera has been working almost perfectly during its first 42 months in orbit. The highly efficient and long term stable camera has led to numerous discoveries in astrophysics. However, from the actual experience some improvements for future missions can be derived:

1. The reduction of intrinsic detector background is very important. While minimum ionizing particles can be discriminated to 100% from the useful X-rays, this is not possible for the particle induced X-ray fluorescence. The X-ray fluorescence can be reduced to about 10^{-4} s^{-1} keV^{-1} cm^{-2}. If that had been already implemented on XMM, the instrument background would have been more than a factor of 10 lower than the cosmic background. A proper graded shielding around the sensitive part of the CCD may lead to the desired improvement.

2. The X-ray optics and the detector should be designed by mechanical and physical means to avoid impacts of micrometeoroids.

3. Future X-ray missions will need larger monolithic focal plane detectors with medium and large pixel sizes (50×50 μm^2 to 1000×1000 μm^2). The energy bandwidth should be extended from 50 eV to 30 keV. The readout time (including the integration time) should be of the order of 1 ms for an array of 10×10 cm^2 with 1000×1000 pixels. Out-of-time events can be suppressed by two orders of magnitude if a frame store concept is implemented, or by the use of dedicated active pixel sensors for X-ray detection.

8. ACKNOWLEDGEMENTS

The XMM focal plane configuration has profited from many discussions with scientists of the Max-Planck-Institut für extraterrestrische Physik and of the MPI-Halbleiterlabor. In particular, we are indebted to Gerhard Lutz, Rainer Richter, and Heinrich Bräuninger. We are grateful to Joachim Trümper for his constant support and numerous discussions over the last 15 years. The frequent discussions with our friends and colleagues from the University of Tübingen, Politecnico di Milano and BNL, New York, were always stimulating. Special thanks to Antonio Longoni, Carlo Fiorini, Marco Sampietro, Emilio Gatti, Pavel Rehak and Eckhard Kendziorra.

REFERENCES

1. E. Gatti and P. Rehak. Semiconductor drift chamber - an application of a novel charge transport scheme. *NIM A*, 225:608 – 621, 1984.
2. L. Strüder, H. Bräuninger, U. Briel, R. Hartmann, G. Hartner, D. Hauff, N. Krause, B. Maier, N. Meidinger, E. Pfeffermann, M. Popp, C. Reppin, R. Richter, D. Stötter, J. Trümper, U. Weber, P. Holl, J. Kemmer, H. Soltau, A. Viehl, and C.v. Zanthier. A 36 cm^2 large Monolythic pn-CCD X-ray Detector for the European XMM Satellite Mission. *Rev. Sci. Ins.*, 68(11):4271 – 4274, 1997.
3. R. Hartmann, L. Strüder, J. Kemmer, P. Lechner, O. Fries, E. Lorenz, R. Mirzoyan. Ultrathin Entrance Windows for Silicon Drift Detectors. *NIM A*, 387(1,2):250 – 254, 1997.
4. L. Strüder et al. The European Photon Imaging Camera on XMM – Newton: The pnCCD camera. *Astronomy and Astrophysics*, 365:18 – 26, 2001.
5. T. Stadlbauer, B. Aschenbach. Spatially Resolved Spectroscopy of Tycho's SNR. *ASP Conf. Series*, 251:276, 2001.
6. D. H. Lumb et al. In-orbit calibration activities of the XMM – Newton EPIC cameras. *SPIE*, 4140:22 – 31, 2000.
7. R. Hartmann, G. Hartner et al. Quantum efficiency of the XMM pn-CCD camera. *SPIE*, 3765:703 – 713, 1999.
8. F. Haberl, U.G. Briel, K. Dennerl, and V.E. Zavlin. Spectral response of the EPIC-PN detector: basic dependences *ESA SP-488*, 2002, in press (astro-ph/0203235). Proc. Symposium 'New Visions of the X-ray Universe in the XMM–Newton and Chandra Era', 26-30 November 2001, ESTEC, the Netherlands.
9. M.J. Freyberg, U.G. Briel, K. Dennerl, F. Haberl, G. Hartner, E. Kendziorra, and M. Kirsch. The XMM–Newton EPIC PN Camera: spectral and temporal properties of the internal background. *ESA SP-488*, 2002. Proc. Symposium 'New Visions of the X-ray Universe in the XMM–Newton and Chandra Era', 26-30 November 2001, ESTEC, the Netherlands.
10. F. Haberl, P.J. Bennie, U.G. Briel, K. Dennerl, P. Ferrando, M. Freyberg, G. Griffiths, J.W. den Herder, D. Lumb, S. Molendi, R.D. Saxton, S. Sembay, and V.E. Zavlin. Cross-calibration of the EPIC MOS and PN cameras on-board XMM–Newton using narrow spectral emission features. *ESA SP-488*, 2002, in press (astro-ph/0203236). Proc. Symposium 'New Visions of the X-ray Universe in the XMM–Newton and Chandra Era', 26-30 November 2001, ESTEC, the Netherlands.
11. N. Meidinger, L. Strüder, H. Soltau, and C.v. Zanthier. Radiation Hardness of pn-CCDs for X-ray Astronomy. *IEEE - NS*, 42(6):2066 – 2073, 1995.
12. C. Fiorini and P. Lechner. Continuous Charge Restoration in Semiconductor Detectors by Means of the Gate-to-Drain Current of the Integrated Front-End JFET. *IEEE - NS*, 46(3):761 – 764, 1999.
13. N. Meidinger et al. First measurements with a frame store PN-CCD X-ray detector. *NIM A, these proceedings.*
14. Bernd Aschenbach. Grazing incidence reflection of protons. *to be published in NIM A*, 2003. Presentation given at the ESA Radiation Damage Meeting on Oct. - 21, 1999 at ESTEC, Noordwijk, the Netherlands.
15. L. Strüder, N. Meidinger, E. Pfeffermann, R. Hartmann, H. Bräuninger, C. Reppin, U. Briel, H. Hippmann, W. Kink, D. Hauff, N. Krause, B. Aschenbach, G. Hartner, K. Dennerl, F. Haberl, D. Stötter, S. Kemmer, J. Trümper, G. Lutz, R.H. Richter, P. Solc, R. Eckart, E. Kendziorra, M. Kuster, C. von Zanthier, P. Holl, A. Viehl, S. Krisch, J. Kemmer, and H. Soltau. X-ray pn-CCDs on the XMM-Newton Observatory. *SPIE*, 4012(85):342 – 352, 2000.

16. M.J. Freyberg, E. Pfeffermann, and U.G. Briel. The XMM–Newton EPIC PN Camera: spatial distribution of the internal background fluorescence lines. *ESA SP-488*, 2002. Proc. Symposium 'New Visions of the X-ray Universe in the XMM–Newton and Chandra Era', 26-30 November 2001, ESTEC, the Netherlands.
17. G. Lutz et al. pnCCDs for Axion search in the CAST experiment. *NIM A*, 2003. to be published.
18. E. Kendziorra, T. Clauß, N. Meidinger, M. Kirsch, M. Kuster, P. Risse, G. Hartner, R. Staubert, L. Strüder. The effect of low energy protons on the performance of the EPIC pn-CCD detector on XMM-Newton. *SPIE*, 4140:32 – 41, 2000.
19. N. Meidinger, B. Schmalhofer, and L. Strüder. Particle and X-ray damage in pn-CCDs. *NIM A*, 439:319 – 337, 2000.
20. L. Strüder et al. Evidence for a micrometeoroid damage in the pn-CCD camera system aboard XMM-Newton. *Astronomy and Astrophysics*, 375:5 – 8, 2001.
21. N. Meidinger, B. Aschenbach, H. Bräuninger, G. Drolshagen, J. Englhauser, R. Hartmann, G. Hartner, R. Srama, L. Strüder, M. Stübig, J. Trümper. Experimental verification of a micrometeoroid damage in the pn-CCD camera system aboard XMM-Newton. *SPIE*, 4851:243 – 254, 2002.